Article:

Patil, D.S., Konale, M., Gabel, M. et al. (6 more authors) (2018) Impact of rare earth ion size on the phase evolution of MoO3-containing aluminoborosilicate glass-ceramics. Journal of Nuclear Materials, 510. pp. 539-550. ISSN 0022-3115

https://doi.org/10.1016/j.jnucmat.2018.08.004

Impact of Rare Earth Ion Size on the Phase Evolution of MoO_3-Containing Aluminoborosilicate Glass-Ceramics

Deepak S. Patil[1,2], Manisha Konale[1,3], Mathew Gabel[4], Owen K. Neill[5], Jarrod Crum[6], Ashutosh Goel[7], Martin Stennett,[8] Neil C. Hyatt,[8] John S. McCloy[1,2,6#]

[1]School of Mechanical & Materials Engineering, Washington State University, Pullman, WA 99164, USA

[2]Materials Science & Engineering Program, Washington State University, Pullman, WA 99164, USA

[3]Department of General and Inorganic Chemistry and CEMNAT, Faculty of Chemical Technology, University of Pardubice, Studentska 95, Pardubice, 53210, Czech Republic

[4]Department of Physics and Astronomy, Washington State University, Pullman, Washington 99164-2814, USA

[5]Electron Microbeam Analysis Lab, School of Earth and Environmental Sciences, University of Michigan, Ann Arbor, Michigan, 48109-1005, USA

[6]Pacific Northwest National Laboratory, P.O. Box 999, Richland, Washington 99352, USA

[7]Department of Materials Science and Engineering, Rutgers – The State University of New Jersey, Piscataway, New Jersey, USA

[8]Department of Materials Science and Engineering, the University of Sheffield, S1 3JD, UK

Corresponding author:

#john.mccloy@wsu.edu; Phone +1 509-335-7796; Fax +1 509-335-4662

Abstract

Transition metal and rare earth cations are important fission products present in used nuclear fuel, which in high concentrations tend to precipitate crystalline phases in vitreous nuclear waste forms. Two phases of particular interest are powellite ($CaMoO_4$) and oxyapatite ($Ca_2RE_8(SiO_4)_6O_2$). The glass compositional dependencies controlling crystallization of these phases on cooling from the melt are poorly understood. In the present study, the effect of rare earth identity and modifier cation field strength on powellite and apatite crystallization were studied in a model MoO_3-containing alkali/alkaline-earth aluminoborosilicate glass with focus on (1) influence of rare earth cation size (for RE^{3+}: Ce, La, Nd, Sm, Er, Yb) and (2) influence of non-framework cations (RE^{3+}, Mo^{6+}, Na^+, Ca^{2+}). Quenched glasses and glass-ceramics (obtained by slow cooling) were characterized by X-ray diffraction (XRD), Raman spectroscopy, X-ray absorption (XAS), and electron probe microanalysis (EPMA). All samples were X-ray amorphous upon quenching, except the Ce-containing composition which crystallized ceria (CeO_2), and the sample devoid of any rare earth cations which crystallized powellite ($CaMoO_4$). On heat treatment, powellite and oxyapatite crystallized in the majority of the samples with the former crystallizing in the volume, while the latter on the surface. The EPMA results confirmed a small concentration of boron in the oxyapatite crystal structure. RE cations were incorporated in the glass, as well as in powellite, oxyapatite, and in the case of Yb^{3+}, keiviite ($Yb_2Si_2O_7$). Raman spectroscopy showed that the primary vibration band for molybdate MoO_4^{2-} in the glasses was strongly affected by the ionic field strength of the modifying cations (alkali, alkaline earth, and RE), suggesting their proximity to the MoO_4^{2-} ions in the glass, though the Mo-O bond length and coordination according to XAS suggested little local change.

Keywords: Rare earth ions**,** nuclear waste immobilization, molybdate, glass-ceramic

1 Introduction

Borosilicate glasses are one of the most suitable matrices for immobilization of nuclear waste worldwide due to their high nuclear waste loading capacity, low tendency for crystallization, high chemical durability, and high self-irradiation resistance [1]. Nuclear waste from reprocessing of used nuclear fuel (UNF) contains a large variety of fission products, including large quantities of the rare-earth (RE) and transition metals (TM), with molybdenum being a particularly problematic due to its high fission yield and low solubility in borosilicate glass [2]. In some countries, the research effort is directed towards the development of glass waste form with no crystallization, or at least minimal crystallization of only durable phases [3]. Another suggested approach being pursued is the development of a glass-ceramic waste form of a desired phase assemblage by controlled crystallization, thus leading to higher waste loading and superior chemical durability in comparison to its glassy counterpart [4-8]. Two crystalline phases of particular interest are powellite ($CaMoO_4$) and oxyapatite (nominally $Ca_2RE_8(SiO_4)_6O_2$), which are the primary crystalline phases accommodating Mo and RE ions in these nuclear waste glass-ceramic systems [5].

1.1 Molybdenum in borosilicate glass and glass-ceramics

In order to design a borosilicate-based glassy waste form, it is imperative to understand the compositional and structural drivers governing the solubility of molybdenum oxides in the relevant glass chemistries. Based on the existing literature [9-11], the solubility of MoO_3 in alkali borosilicate glasses is limited to ~1 mass% when no rare earth ions are present (see below) [12]. This threshold limit of MoO_3 solubility affects the total loading of HLW into the base glass matrix, which leads to the increase of the total volume of the vitrified waste. Depending on the specific waste stream the maximum waste loading may be as low as ~18 mass%. Higher amounts of MoO_3 (>1 mass%) in borosilicate glass is known to induce phase separation and crystallization [10, 13]. The phase separation and crystallization of Mo phases can have a deleterious effect on the durability and safety of the vitrified waste. For compositions rich in alkali, MoO_3 usually phase separates and crystallizes as an alkali molybdate (i.e., Na_2MoO_4) which is soluble in water [14]. Also, the alkali ions in Na_2MoO_4 can be partially or fully replaced by other alkali cations (short-lived ^{137}Cs or long-lived ^{135}Cs) resulting in water-soluble alkali molybdates such as $Cs_3Na(MoO_4)_2$, $CsNaMoO_4 \cdot 2H_2O$ and Cs_2MoO_4 [14-16]. It is known that the distribution of Na^+ in the glass can be controlled, such as with Al_2O_3, B_2O_3 and CaO, thus forcing molybdate to partition and crystallize powellite ($CaMoO_4$) which is more durable in water than alkali molybdates [10, 17].

In alkali borosilicate glasses, the molybdenum cation exists primarily in +6 oxidation state (as molybdate oxyanion), and in the dilute limit as an MoO_4^{2-} tetrahedron, based on evidence from Mo K-edge X-ray absorption [18, 19], and molybdate vibrational frequency changes with the average charge density of modifier [19]. Molybdate oxyanions are thought to be located in the depolymerized region of the glass structure surrounded by alkali and alkaline-earth cations [12]. Recent *ab initio* molecular dynamics simulations have shown that when Li^+ is substituted for Na^+, however, some longer Mo-O bonds result in connection with the borosilicate network and an effective Mo^{5+} charge [20].

1.2 Rare earth cations (RE^{3+}) in borosilicate glass and glass-ceramics

Molybdate and RE ions interact strongly in borosilicate glasses, with the latter exerting a significant impact on the solubility of former (increases to 3 – 5 mass%) in the glass structure [1, 21]. However, the mechanism of their interaction resulting in higher solubility of molybdenum in borosilicate glasses is still debated [11]. The most well-known hypothesis is the close relationship between RE^{3+} and $[MoO_4]^{2-}$ tetrahedral entities in the depolymerized region of the glassy network, where the RE^{3+} ions tend to disperse any molybdate clusters leading to an increase in the molybdenum solubility in the glassy waste form. On the contrary, the removal of RE^{3+} from the glassy matrix (for example, by crystallization of rare-earth containing oxyapatite phase) results in the crystallization of alkali/alkaline-earth molybdate phases [1, 21, 22]. Further, both RE (Nd, Gd, etc.) [10, 23-25] and actinide ions [26] can be incorporated in the powellite crystal structure, as well as the related Na-Nd molybdate scheelite structure [27, 28].

The sequence of crystallization of oxyapatite and powellite is highly dependent on several parameters. Generally, for a glass containing both MoO_4^{2-} and RE^{3+}, the crystallization (upon heating from room temperature) initiates through the formation of powellite in the volume followed by oxyapatite on the surface [21], while this sequence reverses during crystallization from the melt under slow cooling [11]. In fact, molybdate crystalline phases (Na_2MoO_4, $CaMoO_4$) have been suggested as nucleation sites for apatite crystals [21]. However, as mentioned above, this sequence of crystalline phase assemblage is subject to change based on the glass/melt chemistry and thermal conditions.

Most studies of oxyapatite crystallization in nuclear waste glass have focused on Nd_2O_3 as the primary RE oxide addition, and the phase produced is $Ca_2Nd_8(SiO_4)_6O_2$ [1, 2, 4, 29]. The stoichiometry of this phase is variable, with a tendency to be Ca-rich, Nd-poor, and O-poor, i.e., $Ca_{2+x}Nd_{8-x}(SiO_4)_6O_{2-0.5x}$ [30, 31], though likely the stoichiometric range is quite large, including Ca-absent Nd-only versions of the crystal [32]. The $Ca_2Nd_8(SiO_4)_6O_2$ oxyapatite has been well-studied for radiation damage due to its chemical and structural similarity to target phases for actinide immobilization [33, 34].

The composition of RE oxyapatite can be quite variable, and many synthetic pure phase RE oxyapatites have been reported containing Ca (or Ba, Sr, Mg, or Pb), including La, Nd, Sm, Dy, Er, Lu, as well as Y [35]. Several studies have been conducted looking at the compositions of oxyapatites crystallizing from the simulated nuclear waste glass. In complicated starting glass compositions, energy dispersive spectroscopy (EDS) has shown that multiple RE cations, for example, Y^{3+}, La^{3+}, Ce^{3+}/Ce^{4+}, Pr^{3+}, Nd^{3+}, Sm^{3+}, along with alkali (for example, Na^{+}), and alkaline earth ions (for example, Ca^{2+}, Sr^{2+}) can simultaneously incorporate into the oxyapatite structure [5]. In comparing La, Nd, and La+Nd in Na-Ca aluminoborosilicate glasses, it was observed that the amount of RE_2O_3 that could be accommodated in the glass before apatite crystallization was higher for La than Nd, and that overall apatite composition depended on the RE cation present [36].

According to a study conducted on elucidating the effect of the RE identity and heat treatment protocol on the oxyapatite crystallization in a Mo-free Na-Ca aluminoborosilicate glass [37], crystallization behavior of glasses depends on the ionic radii of the rare-earth cation, where the smaller the size of the rare-earth cation, the more sluggish is the tendency towards crystallization. This effect was most pronounced for the smallest sized RE^{3+} ions (Lu^{3+}, Yb^{3+}, Er^{3+}, Y^{3+}), where no crystals were seen on slow cooling of the melt, a minor amount of crystallization was viewable in monolithic samples (under an electron microscope) when heated from room temperature, and crystals in amounts detectable by XRD were obtained only in glass-ceramics produced through nucleation and crystallization in glass powders. Similar results have also been reported by Goel *et al.* [38] for rare-earth containing alkaline-earth aluminoborosilicate glass-ceramics. All oxyapatites large enough to be measured by EPMA were Ca-RE oxyapatites, with mostly the target RE with a minor amount of Nd (included in all samples to facilitate optical absorption measurements). . Of the four RE cations investigated in the study [37], glasses containing Y^{3+} and Er^{3+} showed crystallization of oxyapatite and an unidentified RE “phase P,” while the compositions containing Yb^{3+} and Lu^{3+} showed only the unidentified RE containing phase and no oxyapatite. The authors [37] postulated that the RE in Ca-RE apatite must be close to the size of the Ca^{2+} ion (in CN=9 “4f” or CN=7 “6h” sites in oxyapatite) in order to favor crystallization, which suggests that smaller 3+ cations (Y, Er, Yb, Lu) may not favorably incorporate into the oxyapatite lattice.

This article builds on the aforementioned work, and focuses on the effect of RE cation on aluminoborosilicate glasses containing MoO_3, both from a structural point of view in the quenched glasses and the effects on crystallization upon slow cooling as would be experienced in the glass-ceramic process. Understanding the partitioning of alkali cations towards Mo and RE oxyanions are important considerations for minimizing the formation of poorly durable alkali molybdate crystalline phases. The current study aims to assess the effect of RE cation size on the partitioning of RE ion to molybdate and apatite phases and to ascertain the partitioning of alkali, alkaline earth, and RE ions near molybdate oxyanions.

2 Experimental methods

2.1 Synthesis

2.1.1 Quenched method synthesis

A simplified nuclear waste glass-ceramic composition comprising 12.14 Na_2O – 13.58 CaO – 3.15 ZrO_2 – 3.53 MoO_3 – 5.14 Al_2O_3 – 11.95 B_2O_3– 50.51 SiO_2 (mol%) was chosen as the baseline for this work. The baseline composition above has been derived from the more complex GC-Mo 5.86 glass-ceramic composition being considered for immobilization of a waste stream derived from aqueous reprocessing of UNF [6]. The simplification has been made assuming Na_2O represents the total fraction of alkali oxides (Na_2O+Li_2O+Cs_2O), CaO represents the alkaline-earth oxides (CaO+BaO+SrO), and each RE in the studied series of glasses represents the total rare-earth oxides (Y_2O_3 + La_2O_3 + Ce_2O_3 + Pr_2O_3 + Nd_2O_3 + Sm_2O_3 + Eu_2O_3 +

Gd_2O_3) in the nuclear waste glass-ceramic, on a molar basis. In this work, a series of glasses have been made with varying RE element (RE = La, Ce, Nd, Sm, Er, Yb) with nominal composition 11.54 Na_2O – 12.91 CaO – 2.99 ZrO_2 – 3.36 MoO_3 – 4.93 RE_2O_3 – 4.89 Al_2O_3 – 11.36 B_2O_3 – 48.02 SiO_2 (mol%). These particular RE were chosen due to their prevalence as fission products (La, Ce, Nd, Sm), their possible multivalent nature (Ce), and their small size for contrast (Er, Yb). Additionally, most of the RE have accessible absorption or luminescent transitions for investigating local site symmetry in future studies. Sample names reflect the RE used, i.e., CeNaCaMo, where the Ce glass was batched using CeO_2 precursor but assuming Ce_2O_3 stoichiometry for the batch calculations.

To see the partitioning of alkali and alkaline earth cations towards Mo and/or RE oxyanions, a second series of samples was also synthesized, where certain components have been individually normalized out, such as RE_2O_3, Na_2O + CaO, or MoO_3. The only exception to this formulation is one glass where Na_2O was removed, and an equal molar concentration of CaO was added (i.e., LaCaMo). In this series of glasses, La was used as the RE. In each case the component removed is represented by removing the element from the sample name, e.g., NaCaMo (La_2O_3 removed), LaCaMo (Na_2O removed), LaMo (Na_2O and CaO removed), LaNaCa (MoO_3 removed). Since Al_2O_3, B_2O_3, SiO_2, and ZrO_2 are in all compositions, they are not included in the sample name. Table 1 summarizes the batched compositions of oxides of the glasses being investigated in the present study, in mol% (mass% values are provided in Supplementary Information, Table S-1).

All glasses were prepared by melt quenching. Homogeneous mixture of batches corresponding to 20 g oxides (in accordance with compositions presented in Table 1) were made using the following precursors; Al_2O_3 (Fisher Chemicals), H_3BO_3 99% (Fisher Bioreagents),

$CaCO_3$ 99% (Fisher chemicals), Na_2CO_3 99.5% (Fisher Chemicals), SiO_2 98.6% (MIN-U-SIL®10), ZrO_2 99+% (STREM Chemicals), MoO_3 99.5% (Alfa Aesar), and RE_2O_3 [La_2O_3 99.99% (Acros Organics), Nd_2O_3 99.9% (Alfa Aesar) Sm_2O_3 99.99% (Alfa Aesar), Er_2O_3 99.9% (Alfa Aesar), Yb_2O_3 99.9% (Alfa Aesar), CeO_2 99.9% (Acros Organics)]. The batches were melted in a 90% Pt – 10% Rh crucible at 1300 °C for 2 h followed by quenching the crucible in water at room temperature. The LaMo sample had a higher melting temperature in comparison to other batches. Therefore it was melted at 1600 °C for only 15 min, to avoid the elevated loss of volatile components. The as-synthesized samples were crushed to powder using a tungsten carbide mill and re-melted under the same conditions to ensure homogenization. The re-melt temperature was limited to 1300 °C (including LaMo sample) in order to decrease the volatility and to emulate the targeted operating temperature (~1350 °C) of the cold crucible induction melter (CCIM), in which these glasses would ultimately be melted for making nuclear waste glass-ceramics [6]. After the second melt, the samples inside crucibles were again quenched in water then annealed near their glass transition temperature (i.e., T_g – 20 °C), as determined by thermal analysis to remove any effects of stress. Portions of the glasses were crushed into powder (particle size <125 μm) for x-ray diffraction (XRD) and Raman spectroscopy measurements. It is noteworthy that though the compositional analysis of the as-melted samples was not performed, minimal change in the batched versus melted composition is expected, based on results obtained in our recent study where negligible volatilization was observed from glass melts of similar compositions melted at 1400 – 1500 °C [11].

2.1.2 Slow Cool Heat Treatment

To understand the crystallization behavior for the proposed glass-ceramic waste form, a heat treatment similar to the 1× canister centerline cooling (CCC) profile, given in Crum *et al.*

[6] was used, as shown in Table S-2. To perform the slow cooling experiment, twice melted and quenched samples were crushed to powder and loaded again in a 90% Pt – 10% Rh boat and heated at 10 °C/min to 1300 °C, held for 1 h to ensure melt homogeneity, and then cooled according to the profile given in Table S-2. At 400 °C, (temperature below the glass transition), samples were taken out from the furnace and cooled in air to room temperature. The slowly cooled samples were labeled -X after the corresponding quenched sample name (e.g., ErNaCaMo-X). For characterization purposes, the obtained samples were partly crushed to powder and partly polished in parallel slabs.

2.2 Characterization

Glasses and glass-ceramics were characterized using X-ray diffraction (XRD) with a PANalytical X'Pert Pro using a Cu K_α (1.541874 Å) line with the tube at 45 kV and 40 mA. The data were collected in the 2θ range of 10 – 90° with a step size of 0.05° and dwell of 0.10 s at each step. Six scans were obtained for each sample, and the analyses were performed on the summed results. For quantitative phase analysis purposes, 10 mass% corundum Al_2O_3 (Fisher Chemicals) was added as an internal standard, and quantitative phase analysis was performed using Rietveld refinement and Highscore 4.5 or Topas software. Refinement comparison between two software packages and two operators suggested an estimated fitting error of ~5% (of the baseline value) on the total amorphous fraction, while a larger error of 1/4 – 2/5 of the crystal fraction value on the individual crystalline phases, which ranged from 2 – 20 mass% abundant.

Raman spectra were obtained by using a Renishaw InVia Raman microscope with a 632 nm (red) laser excitation source with acquisition time of 10 sec, and three repeated spectra being summed. To confirm homogeneity, data were collected at multiple points.

Mo K-edge X-ray absorption spectroscopy (XAS) was performed in transmission mode on beam line BL-27 at the PF Ring at the Photon Factory synchrotron facility (Tsukuba, Japan). The PF Ring operates at 2.5 GeV with a 300 mA ring current. Beamline experiment details are provided in the Supplementary Information. Spectra were recorded between 19800 and 21060 eV with energy steps of 2 eV (19800 – 19960), 0.5 eV (19960 – 20060), 2 eV (20060 – 20460), and 4 eV (20460 – 21060). An accumulation time of 1 s step^{-1} was used for all regions. For each sample six spectra were averaged to improve the signal to noise ratio. Spectra were recorded for five glasses and six crystalline standards. The crystalline standards used were: MoO_2 (Sigma Aldrich) containing Mo^{4+} in octahedral coordination, MoO_3 (Sigma Aldrich) containing Mo^{6+} in octahedral coordination, Na_2MoO_4 and three molybdates ($CaMoO_4$, $SrMoO_4$, $BaMoO_4$) which were all synthesized in-house [39] and contain Mo^{6+} in tetrahedral coordination. All standards were confirmed to be phase pure by X-ray diffraction. Samples for XAS were dispersed in PEG with ratios optimized to achieve approximately one absorption length thickness while maintaining a suitable Mo K absorption edge. Data reduction and subsequent analysis was performed using the Demeter suite of programmes (Athena, Artemis, and Hephaestus) [40], where analysis of X-ray Absorption Near Edge Structure (XANES) and Extended X-ray Absorption Fine Structure (EXAFS) analysis were performed, details in the Supplementary Information.

To observe the phase separation, as well as crystalline structure present (if any) in both quenched and heat treated samples, the samples were further analyzed by electron probe microanalysis (EPMA) using a JEOL JXA-8500F field emission electron microprobe equipped with five wavelength-dispersive X-ray spectrometers (WDS). Analytical conditions, counting times, and calibration standards for quantitative WDS analyses may be found in Supplementary

Table S-3. Back-scattered electron (BSE) images and qualitative energy dispersive X-ray spectra (EDS) were also collected using the same electron microprobe.

3 Results and Discussion

3.1 Quenched glasses

3.1.1 Visible observation

As shown in Fig. S-1, all the glasses with 4.93 mol.% (~20 mass%) of RE_2O_3, except CeNaCaMo, were transparent despite containing 3.36 mol.% (~6 mass%) MoO_3. The same composition with RE_2O_3 normalized out (i.e., NaCaMo) was opaque, indicating the importance of RE for enhancing Mo solubility as has been observed by other authors, e.g. [11].

For the CeNaCaMo sample, phase separation in the glass was evident, (Fig. S-1 lower image, showing top and bottom/quench side), and a yellowish phase was noted on the surface which was in contact with the crucible bottom. A brown-colored glassy matrix was present on the top side of this glass. The coloration of Ce-doped borosilicate glasses has been described [41], indicating that 100% Ce^{3+} in a borosilicate glass matrix is hard to achieve, and there is always some Ce^{4+} still present. In general, the color of a Ce-doped borosilicate glass changes from yellow to brown with latter being a characteristic of 4+ oxidation state being dominant. Therefore, the brown-colored glasses observed in the current study indicate a high concentration of Ce in the 4+ state. However, that does not negate the presence of Ce^{3+} in these glasses as it is known from the literature that Ce is always present in both valence states (3+ and 4+) in borosilicate glasses [41-43]. Most other REs, including the other REs in the current study, should only be present in the +3 state in a borosilicate glass [44].

In the second series of glasses, where single components were removed, glasses were white and opaque, except LaNaCa where MoO_3 was removed from the composition (Fig. S-1).

This result suggests that the MoO_3 may be responsible for the opacity in the other samples, i.e., NaCaMo (RE_2O_3 removed), LaCaMo (Na_2O removed), and LaMo (Na_2O and CaO removed). Note that two phases were macroscopically evident in LaCaMo even after re-melt: (i) an opaque white phase and, (ii) a thin transparent layer. The observed opacity is due to light scattering, from either crystalline phases or amorphous phase separation, which was further determined by XRD and microscopy (see below).

3.1.2 SEM and EDS analysis

To ensure homogeneity of the quenched samples as well as to observe phase separation and/or crystalline phases present (if any), samples were analyzed by SEM with BSE images. Also, to check for any volatile element loss, a semi-quantitative EDS point analysis was performed done on a minimum of three different arbitrary spots. The obtained SEM images are shown in Fig. S-3. SEM analyses were consistent with the XRD results, in that crystalline phases were observed in NaCaMo and 493Ce samples. All other samples appeared chemically homogeneous. Even in the cases of LaCaMo and LaMo, despite being visibly opaque and having minor SEM-BSE color contrast, EDS showed nearly identical chemical compositions in all spots. The color contrast was possibly from B-enriched and B-poor phases which could not be detected from EDS. Further discussion is provided in the Supplementary Information.

3.1.3 XRD analysis

All quenched samples in both series were X-ray amorphous (see Fig. 1), except CeNaCaMo from series 1 and NaCaMo from series 2. It was notable that LaCaMo and LaMo from series 2 were visibly opaque yet amorphous by XRD, indicating either a small fraction of crystals below the detection limit of XRD or amorphous phase separation. In the case of the other opaque samples, crystallization appeared to be the cause. The NaCaMo XRD showed powellite ($CaMoO_4$) crystals, and the CeNaCaMo XRD showed Zr-doped ceria ($Ce_{0.9}Zr_{0.1}O_2$) crystals.

To see the influence of re-melting (used to aid homogenization), quantification was performed both after initial melting and after re-melting. In all cases, the fraction of crystalline phases decreased after re-melting. Notably, ceria in the CeNaCaMo sample reduced from ~4.4 mass% to 3.1 mass%. XRD analysis of the LaMo sample after the first melting showed 1.08 mass% of zircon ($ZrSiO_4$) and ~0.12 mass% of quartz (SiO_2), but no crystals were observed after the re-melting. The disappearance of crystal peaks in LaMo sample after re-melting did not, however, produce a transparent sample.

3.1.4 Raman Analysis

Raman spectroscopy was performed to help in understanding the local structure of borosilicate glass, particularly the local vibrational environment of Mo [45]. Raman spectra of all quenched samples after re-melting (Fig. 2) were consistent with the literature data on similar compositions [10, 25, 46]. The main characteristic bands of powellite (Raman spectrum of pure synthetic $CaMoO_4$ added in Fig. 2) at 879, 848, 796, 393 and 322 cm^{-1} exactly matched the bands observed in NaCaMo, indicating good agreement with the XRD results. These five vibrational modes corresponded to the modes of the MoO_4^{2-} tetrahedron [25]. The peak at 879 cm^{-1}, corresponding to the symmetric stretch of the Mo-O bonds in MoO_4^{2-} tetrahedra, was the most intense and characteristic peak for $CaMoO_4$ observed in the glasses and glass-ceramics [45]. NaCaMo contained both Na and Ca, and therefore could theoretically form their respective molybdates (Na_2MoO_4 and $CaMoO_4$). However, Mo crystallizes preferentially with Ca in this system, as indicated by the absence of the characteristic band at 891 cm^{-1} for Na_2MoO_4. The likelihood of formation of Na_2MoO_4 versus $CaMoO_4$ depends upon relative concentrations of various glass components, such as Na_2O, CaO, B_2O_3, and Al_2O_3, as described in the literature [10, 14].

In the case of RE containing samples, the most intense peak was found to be at 914 cm^{-1} or higher wavenumbers. The band at 914 cm^{-1} or higher wavenumbers was also assigned to MoO_4^{2-} tetrahedra symmetric stretching, with the shift of original band from 879 cm^{-1} to 914 cm^{-1} or higher wavenumbers due to the partial replacement of Ca^{2+} by RE^{3+} as the nearest neighbor. It is known from the literature that REs can act as modifiers and compete for non-bridging oxygen (NBO) with monovalent Na^+ and bivalent Ca^{2+} [37, 47, 48]. A Raman band at ~919 cm^{-1} has been observed in a simplified SiO_2-CaO glass, containing a total of <1 mol% Nd_2O_3 plus MoO_3, presumably due to isolated MoO_4^{2-} with nearby Ca^{2+} [49] or available Nd^{3+} located in close proximity to the MoO_4^{2-}. This effect of the RE^{3+} ion on the molybdate oxyanion stretch is further confirmed by the LaMo spectrum. Due to the absence of charge balancing Na^+ and Ca^{2+} cations, La^{3+} cations play the role of charge balancing and occupy all the NBO places, resulting in the characteristic Raman band appearing at even higher wavenumber, 932 cm^{-1}. The origin of this 914 cm^{-1} band from a Ca^{2+}/RE^{3+}- influenced molybdate ion was further confirmed by the absence of this peak in the LaNaCa sample.

Additionally, there is a hump or shoulder at ~879 cm^{-1} which can be observed especially in LaNaCaMo, CeNaCaMo, NdNaCaMo and SmNaCaMo samples, which could be due to partial phase separation of powellite crystals (not detected in XRD) or amorphous-like $CaMoO_4$, with the latter being more likely due to the broad nature of the peak. Alternatively, this lower frequency feature could be due to the antisymmetric stretch of molybdate (ν_3), which is ~60 cm^{-1} lower than the symmetric stretch (ν_1) in molybdate with water ligands [50]. One final possibility is that this mode is due to symmetric stretch of a different Mo-O distance or a slightly different environment, as exemplified by the different vibrational modes expected for Mo-O of different MoO_4^{2-} sites in $Gd_2(MoO_4)_3$, ranging from 959 to 851 cm^{-1} [45]. Even as charge density varies for each RE, the Mo-O stretching frequency of 914 cm^{-1} is similar for RE ions close in size to Ca^{2+} (La^{3+}, Ce^{3+}, Nd^{3+} and Sm^{3+}), whereas for smaller RE ions (Er^{3+} and Yb^{3+}) the band shifts to 922 cm^{-1}, confirming the different local environment around Mo for these smaller RE ions. This shift of Mo-O stretching frequency is due to stronger coupling between MoO_4^{2-} and small RE^{3+} ions, i.e., more Ca^{2+} cations replaced by smaller RE^{3+} ions (Er^{3+} and Yb^{3+}) (see Supplemental Information for more discussion).

In the case of CeNaCaMo, as can be seen from Fig. 2, the most intense band is at 467 cm^{-1}, which is due to the $F2_g$ vibrations of the cubic CeO_2 or $Ce_{0.9}Zr_{0.1}O_2$ [44, 51], and consistent with the XRD results. In addition, there were also other features similar to those found in the other RE-containing glasses, such as a band at 914 cm^{-1}, suggesting that some Ce^{3+} in the glass was participating as a charge compensator around the molybdate. The remaining Ce formed a ceria-rich layer on the bottom surface of the quenched glass (see Fig. S-1). This observation of Ce in dual oxidation state is consistent with the EELS (electron energy loss spectroscopy) study of Ce-doped borosilicate glasses, where it has been observed that the Ce in glassy phase adopts primarily +3 state and the remaining Ce adopts +4 state as CeO_2 nanocrystal phase separated from the glass [41, 52].

While considering the effect of alkali, it is useful to compare of spectra of LaNaCaMo (which includes both Na and Ca) with LaCaMo (only Ca) and LaMo (no Na or Ca). In the LaMo sample, the molybdate band shifts to the highest wavenumber observed (932 cm^{-1}), which can be understood as La^{3+} cation acting as a charge compensator around MoO_4^{2-} due to the absence of Na^+ or Ca^{2+} cations. In the case of LaCaMo, Ca^{2+} or La^{3+} will perform this charge compensator role for molybdate, and for any other species such as on AlO_4^- and BO_4^-. From Fig. S-3, the mean charge density of LaCaMo is slightly lower than that of LaMo. Therefore, a slightly lower Mo-O shift was expected for LaCaMo than LaMo, and for LaCaMo the band at 924 cm^{-1}. This confirmed the association of both La^{3+} and Ca^{2+} surrounding MoO_4^{2-} as a charge compensator. For all studied samples, molybdate asymmetric and symmetric stretching lies in the range of 810 – 840 cm^{-1} and 880 – 930 cm^{-1}, respectively, strongly suggesting that Mo is in the 6+ state in tetrahedral coordination. The octahedral Mo stretching bands of Mo-O terminal bond give Raman vibrations in the range of 960 cm^{-1} – 1000 cm^{-1} [46].

The above results support either of the currently debated structural models about the incorporation of molybdate ions in the glass structure. In the model proposed by Chouard *et al.* [22], MoO_4^{2-} and RE^{3+} are found near to each other in the depolymerized zone. Alternatively, in the model proposed by Bréhault *et al.* [11], MoO_4^{2-} and RE^{3+} are found near each other in a RE-Mo-borate glassy phase. The Raman spectra can only show that MoO_4^{2-} and RE^{3+} are proximal, not whether they are in a silicate, borate, or mixed borosilicate environment. The above results did provide insight into the mechanism of Mo solubility enhancement in the presence of RE^{3+} cations. Since Ca^{2+} cations were replaced by RE^{3+} around MoO_4^{2-}, the MoO_4^{2-} tetrahedral species became more compact, which reduced the possibility of clustering of Mo-O-Mo and $(Ca, Na_2)MoO_4$ formation. Also, due to the trivalent nature of RE^{3+}, it cross-polymerized the borosilicate network, compensating multiple NBOs. This may explain why, even though RE^{3+} and/or Ca^{2+} surrounded MoO_4^{2-}, no rare earth - molybdate crystalline phase (i.e., $REMoO_4$ and/or $RE_xCa_{1-x}MoO_4$) or phase separation was observed in any of the quenched RE-containing samples.

3.1.5 X-ray Absorption Spectroscopy

The Mo XANES spectra for the glasses and the standards are shown in Fig. 3a. There are distinct changes in the spectra as a function of both oxidation state and local coordination environment. To minimize the interference between the pre-edge and edge, the edge position was defined as the energy where the edge jump is equal to 0.8 and there is a pseudo-linear variation between the edge position and the oxidation state as shown in Fig. 3b. There is a small spread of edge position for the $[MoO_4]^{2-}$ (molybdate)-containing reference compounds which is related to residual interference effects from slight differences in the features on the low energy side of the absorption edge and also in the XANES region after the edge. These are related to subtle changes in the local structural environment of the Mo in the reference compounds. The measured position of the absorption edges for the glass samples are given in Table 2; all the values fall within those given for the suite of molybdate reference compounds. The presence of the pre-edge feature in the glass samples is a clear signature of $[MoO_4]^{2-}$ molybdate moieties and consistent with the measured absorption edge position (see Supplementary Information).

In order to investigate the local coordination environment of the Mo in the glass samples the EXAFS region of the spectra were analyzed. The amplitude reduction factor (S_0^2) was therefore determined from fitting the EXAFS data acquired for $CaMoO_4$ using the structural model reported by Hazen *et al*. [53]. The k^2 X(k) and the RDF for $CaMoO_4$ are shown in Fig. S-4 and the fit results are given in Table S-3. The nearest-neighbour Mo-O contribution at approximately 1.35 Å (corresponding to an actual distance of 1.78 once phase shift effects have been taken into account) dominates the RDF although weaker features between 2 and 4 Å are related to contributions from other Mo-O, Mo-Ca, and Mo-Mo correlations. The refined value for the nearest-neighbour (Mo-O) contact distance (1.78 Å ± 0.01) was consistent with the structural information and fitted values reported by Farges *et al.* [54], McKeown *et al.* [19], and Short *et al.* [23].

The k^2 X(k) and the RDF data for the glass samples are shown in Fig. 4 overlaid with the data from the standards. The k^2 X(k) consists of a unique damped sine function whose intensity decreases with increasing k value. This is consistent with the sample being amorphous in character and lacking any long range order beyond the first nearest-neighbour coordination shell. No significant contributions can be seen beyond the first peak in the RDF indicating the Mo atoms are not connected to the borosilicate glass network. From visual inspection it is clear that the molybdenum environments in the glasses are similar to the $[MoO_4]^{2-}$ tetrahedral units in $CaMoO_4$. The glass data were fit with a model consisting of a single nearest-neighbour Mo-O contribution and R, σ^2, and ΔE were allowed to vary while S_o^2 was fixed at 0.73. The fitting results are shown in Table 3 and for all the glasses the refined Mo-O distances are all statistically equivalent to the tetrahedral Mo-O distance in $CaMoO_4$. The fitted k^2 X(k) and the corresponding RDF for LaNaCaMo are shown in Fig. 5 as an example of the quality of the fits for the glass samples. The coordination numbers for the LaNaCaMo, SmNaCaMo, and YbNaCaMo glasses are all statistically equivalent to 4.0 which is also indicative of tetrahedral molybdate environments. The refined coordination numbers for the LaCaMo and LaMo glasses are smaller at 3.2 ± 0.4 and 2.9 ± 0.4, respectively, though this difference from 4.0 may not be significant. Attempts to incorporate contributions into the model from an additional Mo-O shell at a slightly further distance proved unsuccessful even when the number of atoms in the shell was constrained. Adjustment of the weighting of this path in increments of $N = 0.5$ resulted in a progressive increase in the residual R-factor.

3.2 Heat-treated samples

As mentioned earlier, to understand the crystallization behavior in a canister, all samples were slow cooled from the melt and further analyzed. Fig. S-2 shows selected samples after heat treatment, all of which became opaque, as expected from crystallization and consequent light scattering.

3.2.1 Electron Micrographs

Electron microscopy (backscattered electron, BSE, images) and microanalysis were used to observe the microscopic structure of crystalline phases grown during slowly cooled heat treatment of the samples. The obtained morphology of some selected samples is shown in Fig. 6. Further images and an extended discussion are provided in Fig. S-7.

In general, powellite crystals were present in all RENaCaMo-X plus NaCaMo-X and LaCaMo-X samples, generally in a cross-like structure. The only Mo-containing sample which did not show powellite was LaMo, which on heat treatment showed multiple complex phase separation. Powellites in this morphology have been observed in previous nuclear glass-ceramic studies [6].

Oxyapatite crystals were observed for all RENaCaMo-X plus LaNaCa-X (Fig S-7a). In YbNaCaMo-X, apatites were difficult to distinguish. No apatites could be seen in LaCaMo-X or LaMo-X. Most oxyapatite crystals observed had skeletal morphology (like in [6]), while some of them were arranged in flower-like structures with faceted morphology or tree/pyramidal structures (similar to structures observed in [1, 55]). Needle-like oxyapatites are also seen, depending on the orientation of the crystal, as seen in the literature [1, 4, 21, 37]. The presence of multiple morphologies indicates that both short- and long-range diffusion or short-range and melt-crystal interface mechanisms are responsible for this type of distribution and growth of crystals [56]. Similar skeletal and pyramidal structures were observed in other glass-crystallization studies with Nd and Mo-containing borosilicate glass-ceramics [6, 37].

Additionally, LaNaCaMo-X indicated that oxyapatite crystals were surface nucleated whereas powellite crystals grew in the bulk matrix. This was confirmed by repeated polishing of the samples and subsequent imaging (not shown), where it was observed that oxyapatite crystals were removed with polishing whereas powellite crystals were still found in the matrix.

In the case of CeNaCaMo-X, ceria crystals were present (intense white phase) with powellite as another phase (gray crosses similar to earlier images). Surprisingly, no apatite phase was observed, though the small amount observed from XRD (see below) may have been polished off during sample preparation.

In the case of YbNaCaMo-X, as observed from XRD, in addition to powellite and oxyapatite crystalline phases, one additional phase is observed – keiviite ($Yb_2Si_2O_7$). Since the elemental composition of both oxyapatite and keiviite are the same (Yb, Si, O), the contrast of both phases in microprobe images are nearly same, so they are difficult to distinguish by this means. However, from XRD analysis (see below), oxyapatite phase fraction is much smaller compared to keiviite, so observed dendrite clusters (shown in Fig. 6) are likely keiviite. Probably keiviite is the unidentified phase produced in Yb- and some Er-containing glass-ceramics previously reported [37].

In LaCaMo-X, replacing Na^+ with Ca^{2+} shows a dramatic influence on heat treatment behavior. Powellite still formed, mostly in chains with some crosses, but there is the formation of an additional flower-like SiO_2 phase in the sample (dark phase in BSE image), which is presumably amorphous according to XRD. It is significant to note that, even though Na^+ is not needed in the typically observe Ca-RE oxyapatite phase, its absence in the glass composition shows prevention of oxyapatite formation.

In the absence of both Na^+ and Ca^{2+} in LaMo-X, the main result of heat treatment was multiple large-scale glass-in-glass phase separations. In this case, no powellite or oxyapatite crystals were observed, but a small fraction of zircon was identified by XRD. These zircon crystals can be seen in the micrographs as black spots inhomogeneously distributed in the matrix producing a gray color (for more clarity, see Fig. S-8d mapping image with Zr distribution). Another white/gray phase present was a B, Mo and La-rich amorphous phase, and the dark phase was a Si-rich amorphous phase. This clearly showed the importance of Na^+ and/or Ca^{2+} for the powellite and oxyapatite formation. The most significant aspect of this sample was the identification of what appears to be a B-Mo-La amorphous phase (see Fig. S-8d) predicted in the recently discussed theory of Bréhault *et al*. [11].

3.2.2 XRD phase analysis

All heat-treated glasses formed at least one crystalline phase, as seen from XRD patterns (Fig. 7). The obtained crystalline phases and quantified relative amounts from Rietveld refinement are shown in Table 4. The actual Rietveld refinement fitting of each sample is shown in Fig. S-6. From the quantitative values of RENaCaMo-X, it was observed that a non-linear trend in the amount of each phase was found moving smaller in RE ion size from LaNaCaMo-X to YbNaCaMo-X. The amount of amorphous phase first increases up to NdNaCaMo-X and subsequently decreases, while crystalline phases (i.e., powellite and oxyapatite) both decrease then increase. There were small deviations in this trend due to additional crystal phases being formed in CeNaCaMo-X (ceria) and YbNaCaMo-X (keiviite, $Yb_2Si_2O_7$) in addition to oxyapatite and powellite.

Note that the oxyapatite phase obtained initially by the fitting software in each case is somewhat different. In the LaNaCaMo-X, the oxyapatite selected as the best fit was $La_{8.9}Si_6O_{25.9}$, which contained no Ca. Note that this phase was also formed in the LaNaCa-X glass. However, after analysis of the microprobe data (see below) it was shown that Ca was invariably present in apatite found. Therefore, all the apatites were analyzed as $Ca_2RE_8Si_6O_{26}$ for quantification, where RE=La^{3+}, Ce^{3+}, Nd^{3+}, Sm^{3+}, Er^{3+}, or Yb^{3+}.

3.2.3 Raman analysis

The Raman spectra obtained after heat treatment complements the XRD data. As shown in Fig. 8, in all samples except LaNaCa-X, CeNaCaMo-X and LaMo-X, characteristics peaks of powellite ($CaMoO_4$) were seen, i.e., the symmetric Mo-O stretching band at 879 cm^{-1} and asymmetric band at 847 cm^{-1}, 794 cm^{-1}, 393 cm^{-1} and 322 cm^{-1}. Despite the presence of oxyapatite as shown in XRD results (Fig. 7 and Table 4), only powellite characteristics peaks appeared in Raman spectra, except in the case of ErNaCaMo-X. This may be due to the lower sensitivity of oxyapatite and higher sensitivity of powellite to the Raman exciting wavelength, so due to the much higher intensity of powellite peaks, the oxyapatite peaks were suppressed.

In the case of ErNaCaMo-X, the appearance of oxyapatite peaks with powellite peaks was due to the decrease of relative intensity of powellite peaks. The powellite characteristic intense peak (i.e., the symmetric Mo-O stretching peak of MoO_4^{2-} tetrahedra at 879 cm^{-1}) in ErNaCaMo-X appeared broader than powellite peaks in other samples (see Fig. 8). This broadening may be due to disordered powellite crystals or additional amorphous $CaMoO_4$. From XRD results in Fig. 7, the presence of comparatively broadened peaks of $CaMoO_4$ confirms that the $CaMoO_4$ crystals are very small, as seen in the electron micrographs.

In the case, where Mo was removed (LaNaCa-X) only oxyapatite peaks were found, and when RE was removed (NaCaMo-X) only Raman peaks corresponding to powellite were found, in agreement with XRD results. In LaNaCa-X Raman data, due to strong fluorescence (possibly from Eu impurity), data above 1200 cm^{-1} has been removed to better view intensity of other bands. In LaNaCa-X, the band at 856 cm^{-1} is due to symmetric stretching vibrations of Si-O species. The lower wavenumber bands (706 cm^{-1}, 530 cm^{-1} and 402 cm^{-1}) are due to asymmetric and bending vibration modes of Si-O. The stretching modes of La-O have been assigned in literature at further lower wavenumber, i.e. between 268 – 280 cm^{-1} [57]. All the peaks of LaNaCa-X were consistent and assigned according to the Guillot *et al.* [57] observations of $La_{8.9}Si_6O_{25.9}$.

Similar to the CeNaCaMo sample before heat treatment, in CeNaCaMo-X the Raman data showed an intense peak of ceria ($Ce_{0.9}Zr_{0.1}O_2$). Due to the very high intensity of the $F2_g$ vibration bands of the cubic ceria, all other characteristics peaks of other phases observed in XRD (i.e., powellite and apatite) were not observed.

In LaCaMo Raman data in Fig. 2, the Mo-O vibration peak appeared at higher wavenumber than RENaCaMo samples, so some differences in the heat treated sample were expected. However, in LaCaMo-X the Raman behavior obtained was similar to RENaCaMo-X samples in showing only powellite peaks.

In the case of LaMo-X, as expected from XRD analysis in Fig. 7, no powellite characteristics peaks were observed. However, numerous new sharp bands at 1011 cm^{-1}, 976 cm^{-1}, 440 cm^{-1} and 359 cm^{-1} were obtained, as shown in Fig. 8. Both 1011 cm^{-1} and 976 cm^{-1} were assigned to $[SiO_4]^{4-}$ group stretching, the former to antisymmetric stretching with B_{1g} symmetry (ν_3), and the latter to ν_1 stretching [58]. The bands at 440 cm^{-1} and 359 cm^{-1} were bending modes ν_2 and ν_4 of the same $[SiO_4]^{4-}$ group. The bending mode vibrations peak intensity was expected to be higher than stretching vibrations due to higher Si-O ionic character, as shown by Dawson *et al.* [59]. In XRD, the crystal phase was identified as zircon ($ZrSiO_4$), which has been observed in some other studies of similar compositions [60, 61]. The broad bands ~ 927 cm^{-1}, 861 cm^{-1}, 708 cm^{-1}, 402 cm^{-1} were probably from different borate structures such as pentaborate (~ 927 cm^{-1}) [62]. The borate was present in the remaining amorphous matrix, as shown in the microscopy.

3.2.4 Quantitative EPMA analysis

To understand the exact chemical composition of each crystalline phase as well as the overall distribution of certain elements in the matrix, all the samples were characterized by WDS point analysis on the EPMA system. In several cases, EPMA mapping was also performed (see Fig S-6). Quantitative analysis of crystal phases was determined in heat-treated glasses for crystals in that were big enough to scan.

Powellite compositions were determined (Table 5) for NaCaMo-X, LaNaCaMo-X, NdNaCaMo-X, and ErNaCaMo-X. Despite the fact that ErNaCaMo-X powellite crystals were overall smaller in size, some crystals of ~1 μm in size were found which were big enough for spot analysis. An apparent trend was observed with RE^{3+} ion size, where La, Nd, and Er samples progressively have less RE and Na and more Ca and Mo in them. This did not appear to be due to interaction volume including surrounding glass but may be due to size and valence compensation of the RE with Na. The sample with no RE (NaCaMo-X) appeared to have essentially no Na, and a similar amount of Mo to the ErNaCaMo-X sample, though the total for quantification was slightly low. By converting mass fractions of oxides into stoichiometry, the measured powellites were (ignoring SiO_2 and Al_2O_3, based on 4 atoms of O per formula unit) approximately $Ca_{0.79}Na_{0.14}La_{0.11}Mo_{1.04}O_4$ (LaNaCaMo), $Ca_{0.88}Na_{0.08}Nd_{0.09}Mo_{1.03}O_4$ (NdNaCaMo), $Ca_{0.90}Na_{0.05}Er_{0.04}Mo_{1.02}O_4$ (ErNaCaMo), and $Ca_{0.96}Mo_{1.01}O_4$ (NaCaMo). Previous EDS measurements of powellites in more complex glasses have shown substitution of alkali (Na, Rb) and alkaline earth (Sr, Ba) [5, 6] and RE [10, 23-25]. This compositional change with RE size was consistent with the fact that as RE^{3+} ion size decreases, the volume of the MoO_4^{2-} tetrahedra decrease and become more isolated, hence it is easier for Ca^{2+} to interact with them to form powellite during slow cooling. All these results were consistent with WDS compositional maps shown in Fig S-8.

Oxyapatite phases were also measured (Table 6), for the RENaCaMo-X (RE=La, Nd, Sm, Er). For the CeNaCaMo-X and YbNaCaMo-X, apatites were not found to be big enough to measure reliably. The LaNaCa-X apatites were also measured, along with the YbNaCaMo-X keiviite crystals.

For the quantification, apatite and keiviite in YbNaCaMo-X were difficult to distinguish by electron imaging. Therefore, an average EPMA composition showed much higher SiO_2 and lower CaO than other apatites likely from the greater contribution of the keiviite phase. Keiviite crystals were very small and narrow, and interaction of the beam with the underlying glass is likely, as suggested from the higher amounts of ZrO_2 and Al_2O_3 measured. For the keiviite crystals, for pure stoichiometric $Yb_2Si_2O_7$ one would expect 76 mass% Yb_2O_3 and 24 mass% SiO_2; clearly, from the analysis, the RE is far too low, and other elements are shown suggesting that some Yb-oxyapatite and/or some residual glass was sampled as well, or that there is considerable substitution in this phase.

The overall inclusion of non-typical oxyapatite elements is worth discussing. In no case was MoO_3 observed in these apatites. The ZrO_2 content was small but measurable and probably real, but could also be interaction with surrounding glass. Al_2O_3 and Na_2O contents were very small or zero. Although quantification of low boron concentrations by EPMA is not entirely reliable due to poor counting statistics from boron's low X-ray yield and the fluorescence of boron in the WDS diffracting crystal [63], the EPMA data indicates that, qualitatively, some small amounts of B_2O_3 (~1-5 mass%) are being incorporated into the oxyapatite phases. This is not unexpected crystallographically [35] and is consistent with previous glass-ceramic studies [64].

Assuming that boron would go on the Si site and Zr would go on the Ca/RE site and not accounting for any excess or deficient oxygen, the approximate stoichiometries can be estimated as: $Ca_{2.8}La_{6.3}Zr_{0.1}Si_{5.2}B_{1.4}O_{26}$ (LaNaCa), $Ca_{2.8}La_{6.5}Zr_{0.1}Si_{5.2}B_{1.3}O_{26}$ (LaNaCaMo), $Ca_{2.7}Nd_{6.7}Zr_{0.1}Si_{5.3}B_{1.1}O_{26}$ (NdNaCaMo), and $Ca_{2.8}Sm_{6.5}Zr_{0.2}Si_{5.3}B_{0.9}O_{26}$ (SmNaCaMo); (apatites for Er and Yb were small, and the compositions are questionable). Overall, Ca levels are higher than the 2 moles assumed in the XRD quantification, but clearly Ca is present and not completely vacant with only the RE participating with vacancies. This small composition difference should not affect the XRD phase quantification. Thus the main oxyapatite constituent concentrations do seem to vary slightly with RE ion size. As observed in Table 6, the Si concentration decreased with RE^{3+} ion size decrease (La, Nd, Sm, Er). This appears to correlate with an increasing concentration of ZrO_2 observed in these samples with decreasing RE ion size. These changes were small and may not be statistically significant, and the ZrO_2 could be a result of interaction with underlying glass, but this could not be definitively determined.

Additionally, the unit cell size of refined oxyapatite and powellite phases was determined from Rietveld analysis of the XRD data, and compared to the RE^{3+} radii (Shannon [65] crystal radii for coordination number 8) in Fig. 9. It can be seen that there is a general trend that with increasing radius of the RE, the unit cell volume of the refined phase increases. It should be noted here that it was possible, then, to predict the presence of RE in both these phases even if the crystals themselves were too small or scarce for EPMA quantification, such as was the case for Yb and Ce apatites and Yb, Sm, and Ce powellites. It is recognized that the coordination number of the RE in apatite would likely be 7 or 9 due to the apatite crystal structure, but coordination number 8 was chosen as representative, and the trends are the same. The analysis for oxyapatite should be valid given that the total amount of RE present in the analyzed oxyapatite phase was approximately the same (26 – 28 mol% for all but the Er and Yb samples). and the main variable in lattice volume should come from the size difference or at least a proxy for lattice strain in which other substitutions are made. For the powellites the situation is somewhat more complicated, in that multiple concentrations are changing (RE, Mo, Na, Ca), but at least qualitatively the RE cation size does appear to trend with the lattice volume.

4 Conclusions

This study revealed the complex influence of RE^{3+} ion size on crystallization behavior in Mo- and RE-containing simulated nuclear waste glass-ceramics. A key factor contributing to the solubility of MoO_3 in these glasses was the presence of RE^{3+} cations and the isolation of MoO_4^{2-} tetrahedra due to the high field strength of the RE. The slow-cooling from the melt of samples missing alkali and/or alkaline earth cations (LaCaMo-X and LaMo-X), it was clear that both Na^+ and Ca^{2+} cationic species were required for the formation of oxyapatite, even though Na is not present in any significant quantity in the crystal. This is despite the fact that theoretically as well as experimentally oxyapatite formation is possible without these cation species ($\sim RE_{10}Si_6O_{26}$), such as in the case of $La_{10-x}Vac_x(SiO_6)_4O_{2\pm\delta}$, where ‘Vac’ indicates cation vacancies [57, 64].

Several important conclusions can be made from the study of interactions between RE and Mo in aluminoborosilicate systems with and without alkali and alkaline earths. From the XRD results of samples before heat treatment, it is shown that even ~6 mass% of MoO_3 can be dissolved in the presence of ~20 mass% of RE_2O_3 without powellite crystallization. A key factor of solubility of MoO_3 in the presence of RE^{3+} cations is the isolation of MoO_4^{2-} tetrahedron due to the high field strength of RE^{3+} cations, as confirmed by Raman analysis. RE^{3+} cationic size has a non-linear influence of on crystallization behavior of the studied samples, probably due to a threshold value of charge density of RE^{3+} cations (i.e., in the studied case for smaller cations Er^{3+} and Yb^{3+}), after which the coupling interaction between borosilicate network and these (Er^{3+} and Yb^{3+}) cations behaves differently in the glassy matrix. The smallest RE studied, Yb, tends to crystallize only a small amount of apatite but a large amount of the RE silicate keiviite.

Fundamental relationships between the Mo and RE in the glasses and glass-ceramics have been clarified. In all studied glasses the tetrahedral nature of MoO_4^{2-} and its +6 state are further confirmed from Raman and XAS analysis, and all REs studied in are in the +3 state, except Ce which is present in both +3 and +4. RE cations are near Mo in the glass, with higher field strength cations changing the vibrational frequency in samples with different sized RE and those without Na^+ and/or Ca^{2+}. Additionally, some RE appears to partition to the Ca molybdate powellite crystalline phases (Ca, RE, Na)MoO_4, with smaller RE substituting to a lesser extent, Na content generally trending with RE in powellite, and Mo possibly being deficient when RE contents are high.

Acknowledgements

This research is being performed using funding received from the U.S. Department of Energy – Office of Nuclear Energy through the Nuclear Energy University Program under the award DE-NE0008431. The authors would like to thank Antoine Bréhault, Muad Saleh, Prashant Rajbhandari, and Russell J. Hand for helpful conversations and comments. Thanks to Jacob Peterson and Brian Riley for providing the alkaline earth molybdates for XAS standards.

References

[1] N. Chouard, D. Caurant, O. Majérus, N. Guezi-Hasni, J.-L. Dussossoy, R. Baddour-Hadjean and J.-P. Pereira-Ramos, J. Alloys Compd. 671 (2016) 84-99.

[2] D. Caurant, P. Loiseau, O. Majerus, V. Aubin-Chevaldonnet, I. Bardez and A. Quintas, Glasses, Glass-Ceramics and Ceramics for Immobilization of Highly Radioactive Nuclear Wastes, Nova Science Publishers, Inc., New York (2009).

[3] A. Quintas, D. Caurant, O. Majérus, P. Loiseau, T. Charpentier and J.-L. Dussossoy, J. Alloys Compd. 714 (2017) 47-62.

[4] J. V. Crum, L. Turo, B. Riley, M. Tang and A. Kossoy, J. Am. Ceram. Soc. 95 (2012) 1297-1303.

[5] J. V. Crum, J. J. Neeway, B. J. Riley, Z. Zhu, M. J. Olszta and M. Tang, J. Nucl. Mater. 482 (2016) 1-11.

[6] J. Crum, V. Maio, J. McCloy, C. Scott, B. Riley, B. Benefiel, J. Vienna, K. Archibald, C. Rodriguez, V. Rutledge, Z. Zhu, J. Ryan and M. Olszta, J. Nucl. Mater. 444 (2014) 481-492.

[7] O. Pinet, J. L. Dussossoy, C. David and C. Fillet, J. Nucl. Mater. 377 (2008) 307-312.

[8] J. McCloy and A. Goel, MRS Bull. 42 (2017) 233-240.

[9] Y. Kawamoto, K. Clemens and M. Tomozawa, J. Am. Ceram. Soc. 64 (1981) 292-296.

[10] D. Caurant, O. Majérus, E. Fadel, A. Quintas, C. Gervais, T. Charpentier and D. Neuville, J. Nucl. Mater. 396 (2010) 94-101.

[11] A. Brehault, D. Patil, H. Kamat, R. E. Youngman, L. M. Thirion, J. C. Mauro, C. L. Corkhill, J. S. McCloy and A. Goel, J. Phys. Chem. B 122 (2018) 1714-1729.

[12] G. Calas, M. Le Grand, L. Galoisy and D. Ghaleb, J. Nucl. Mater. 322 (2003) 15-20.

[13] N. Henry, P. Deniard, S. Jobic, R. Brec, C. Fillet, F. Bart, A. Grandjean and O. Pinet, J. Non-Cryst. Solids 333 (2004) 199-205.

[14] D. Caurant, O. Majérus, E. Fadel, M. Lenoir, C. Gervais and O. Pinet, J. Am. Ceram. Soc. 90 (2007) 774-783.

[15] C. Martineau, V. K. Michaelis, S. Schuller and S. Kroeker, Chem. Mater. 22 (2010) 4896-4903.

[16] B. J. Greer and S. Kroeker, Phys. Chem. Chem. Phys. 14 (2012) 7375-7383.

[17] M. Magnin, S. Schuller, C. Mercier, J. Trébosc, D. Caurant, O. Majérus, F. Angéli and T. Charpentier, J. Am. Ceram. Soc. 94 (2011) 4274-4282.

[18] N. C. Hyatt, R. J. Short, R. J. Hand, W. E. Lee, F. Livens, J. M. Charnock and R. L. Bilsborrow, The Structural Chemistry of Molybdenum in Model High Level Nuclear Waste Glasses, Investigated by MO K-Edge X-Ray Absorption Spectroscopy. Environmental Issues and Waste Management Technologies in the Ceramic and Nuclear Industries X, John Wiley & Sons, Inc. (2006).

[19] D. A. McKeown, H. Gan and I. L. Pegg, J. Nucl. Mater. 488 (2017) 143-149.

[20] K. Konstantinou, P. V. Sushko and D. M. Duffy, Phys. Chem. Chem. Phys. 18 (2016) 26125-26132.

[21] N. Chouard, D. Caurant, O. Majérus, J. L. Dussossoy, S. Klimin, D. Pytalev, R. Baddour-Hadjean and J. P. Pereira-Ramos, J. Mater. Sci. (2014) 1-23.

[22] N. Chouard, D. Caurant, O. Majérus, J. L. Dussossoy, A. Ledieu, S. Peuget, R. Baddour-Hadjean and J. P. Pereira-Ramos, J. Non-Cryst. Solids 357 (2011) 2752-2762.

[23] R. J. Short, R. J. Hand, N. C. Hyatt and G. Möbus, J. Nucl. Mater. 340 (2005) 179-186.

[24] T. Taurines and B. Boizot, J. Non-Cryst. Solids 357 (2011) 2723-2725.

[25] T. Taurines, D. Neff and B. Boizot, J. Am. Ceram. Soc. 96 (2013) 3001-3007.

[26] D. Bosbach, T. Rabung, F. Brandt and T. Fanghänel, Radiochim. Acta 92 (2004) 639-643.

[27] E. Kashchieva, I. Petrov, L. Aleksandrov, R. Iordanova and Y. Dimitriev, Phys. Chem. Glasses 53 (2012) 264-270.

[28] A. Kossoy, R. Schulze, M. Tang, D. J. Safarik and R. J. McCabe, J. Nucl. Mater. 437 (2013) 216-221.

[29] D. Caurant, O. Majerus, P. Loiseau, I. Bardez, N. Baffier and J. L. Dussossoy, J. Nucl. Mater. 354 (2006) 143-162.

[30] A. Quintas, O. Majérus, D. Caurant, J.-L. Dussossoy and P. Vermaut, J. Am. Ceram. Soc. 90 (2007) 712-719.

[31] T. H. Le, N. R. Brooks, K. Binnemans, B. Blanpain, M. Guo and L. Van Meervelt, Acta Cryst. E 72 (2016) 209-211.

[32] N. Christensen, R. G. Hazell and A. W. Hewat, Acta Chem. Scandan. 51 (1997) 37-43.

[33] W. J. Weber, Radiation Eff. 77 (1983) 295-308.

[34] W. J. Weber and R. B. Greegor, Nucl. Instr. Meth. B 46 (1990) 160-164.

[35] J. Ito, Amer. Mineral. 53 (1968) 890-907.

[36] A. Kidari, J.-L. Dussossoy, E. Brackx, D. Caurant, M. Magnin and I. Bardez-Giboire, J. Am. Ceram. Soc. 95 (2012) 2537-2544.

[37] A. Quintas, D. Caurant, O. Majerus, J. L. Dussosoy and T. Charpentier, Phys. Chem. Glasses 29 (2008) 192-197.

[38] A. Goel, A. A. Reddy, M. J. Pascual, L. Gremillard, A. Malchere and J. M. F. Ferreira, J. Mater. Chem. 22 (2012) 10042-10054.

[39] J. A. Peterson, J. V. Crum, B. J. Riley, R. M. Asmussen and J. J. Neeway, J. Nucl. Mater. under review (2018).

[40] B. Ravel and M. Newville, J. Synchr. Rad. 12 (2005) 537-541.

[41] M. Shiratori, Ultraviolet-absorbing glass tube for fluorescent lamp and glass tube comprising the same for fluorescent lamp, USPTO, US 20090280277 A1 (2009).

[42] B. Yale and K. M. Fyles, Borosilicate glass compositions incorporating cerium oxide, USPTO, US 5017521 A (1991).

[43] Z. Wang and L. A. Cheng, Phys. Chem. Glasses 55 (2014) 182-189.

[44] P. Sudarsanam, B. Mallesham, D. N. Durgasri and B. M. Reddy, RSC Adv. 4 (2014) 11322-11330.

[45] F. D. Hardcastle and I. E. Wachs, J. Raman Spectrosc. 21 (1990) 683-691.

[46] L. Aleksandrov, T. Komatsu, R. Iordanova and Y. Dimitriev, J. Phys. Chem. Solids 72 (2011) 263-268.

[47] J. A. Johnson, C. J. Benmore, D. Holland, J. Du, B. Beuneu and A. Mekki, J. Phys. Cond. Matt. 23 (2011) 065404.

[48] M. Wilding, Y. Badyal and A. Navrotsky, J. Non-Cryst. Solids 353 (2007) 4792-4800.

[49] M. Magnin, S. Schuller, D. Caurant, O. Majérus, D. d. Ligny and C. Mercier, Effect of Compositional Changes on the Structure and Crystallization Tendency of a Borosilicate Glass Containing MoO3. Environmental Issues and Waste Management Technologies in the Materials and Nuclear Industries XII, John Wiley & Sons, Inc. (2009).

[50] N. Weinstock and H. Schulze, J. Chem. Phys. 59 (1973) 5063-5067.

[51] T. Taniguchi, T. Watanebe, S. Ichinohe, M. Yoshimura, K.-i. Katsumata, K. Okada and N. Matsushita, Nanoscale 2 (2010) 1426-1428.

[52] G. Yang, R. Hand and G. Möbus, J. Phys. Conf. Ser. 126 (2008) 012021.

[53] R. M. Hazen, L. W. Finger and J. W. E. Mariathasan, 46 (1985) 253-263.

[54] F. Farges, R. Siewert, G. E. Brown, A. Guesdon and G. Morin, Canad. Mineral. 44 (2006) 731-753.

[55] A. Quintas, D. Caurant, O. Majérus, T. Charpentier and J. L. Dussossoy, Mat. Res. Bull. 44 (2009) 1895-1898.

[56] R. J. Kirkpatrick, Amer. Mineral. 60 (1975) 798-814.

[57] S. Guillot, S. Beaudet-Savignat, S. Lambert, P. Roussel, G. Tricot, R.-N. Vannier and A. Rubbens, J. Raman Spectrosc. 42 (2011) 1455-1461.

[58] A. Gucsik, M. Zhang, C. Koeberl, E. K. H. Salje, S. A. T. Redfern and J. M. Pruneda, Mineral. Mag. 68 (2004) 801-811.

[59] P. Dawson, M. M. Hargreave and G. R. Wilkinson, J. Phys. C Solid State Phys. 4 (1971) 240.

[60] S. Schuller, O. Pinet, A. Grandjean and T. Blisson, J. Non-Cryst. Solids 354 (2008) 296-300.

[61] S. Schuller, O. Pinet and B. Penelon, J. Am. Ceram. Soc. 94 (2011) 447-454.

[62] G. Padmaja and P. Kistaiah, J. Phys. Chem. A 113 (2009) 2397-2404.

[63] J. J. McGee and L. M. Anovitz, Electron probe microanalysis of geologic materials for boron. In: L. M. Anovitz and E. S. Grew, Editors, Reviews in Mineralogy, Petrology and Geochemistry, Mineralogical Society of America, Chantilly, VA (1996).

[64] L. Li, D. M. Strachan, H. Li, L. L. Davis and M. Qian, J. Non-Cryst. Solids 272 (2000) 46-56.

[65] R. D. Shannon, Acta Crystallog. A 32 (1976) 751-767.

Tables

Table 1. Chemical compositions of the target samples in mol%.

Sample Name	RE_2O_3	Na_2O	CaO	MoO_3	SiO_2	B_2O_3	Al_2O_3	ZrO_2
NaCaMo	-	12.14	13.58	3.53	50.51	11.95	5.14	3.15
LaNaCaMo	4.93	11.54	12.91	3.36	48.02	11.36	4.89	2.99
CeNaCaMo	4.93	11.54	12.91	3.36	48.02	11.36	4.89	2.99
NdNaCaMo	4.93	11.54	12.91	3.36	48.02	11.36	4.89	2.99
SmNaCaMo	4.93	11.54	12.91	3.36	48.02	11.36	4.89	2.99
ErNaCaMo	4.93	11.54	12.91	3.36	48.02	11.36	4.89	2.99
YbNaCaMo	4.93	11.54	12.91	3.36	48.02	11.36	4.89	2.99
LaCaMo	4.93	-	24.45	3.36	48.02	11.36	4.89	2.99
LaMo	6.53	-	-	4.45	63.56	15.04	6.47	3.96
LaNaCa	5.10	11.94	13.36	-	49.69	11.75	5.06	3.10

Table 2. Mo K-edge energy (defined as the energy where the edge jump is equal to 0.8) and average oxidation state for reference standards and glass samples.

Sample name	K-edge energy (eV)	Mo Ox. state
Mo metal	20010.0	0
MoO_2	20015.2	4
MoO_3	20018.9	6
Na_2MoO_4	20020.4	6
$BaMoO_4$	20019.8	6
$SrMoO_4$	20019.0	6
$CaMoO_4$	20018.5	6
LaNaCaMo	20019.3	6
SmNaCaMo	20019.2	6
YbNaCaMo	20019.3	6
LaCaMo	20018.8	6
LaMo	20018.6	6

Table 3. Structural parameters for glass samples obtained from the Mo K-edge fits. $R_{Mo\text{-}i}$ is the average interatomic distance for a given pair (Mo-i) of atoms. σ^2_i is the Debye-Waller factor (estimated from the distribution of bond lengths) and $N_{Fe\text{-}i}$ is the refined number of scattered in the coordination shell. The refined amplitude reduction factor (S_0^2) determined from fitting of the $CaMoO_4$ data was fixed at 0.73. The fit range in k space was from 1.75 to 15.5 Å^{-1} and in R space from 1.0 to 6.0 Å. The number of independent variables (N_v) and independent data points (N_{ip}, determined from the Nyquist theorem) was $N_v = 4$ and $N_{ip} = 43$, respectively.

Sample name	E_0 (eV)	±	$R_{Mo\text{-}O1}$ (Å)	±	$N_{Mo\text{-}O1}$	±	σ^2 (Å2)	±	R-factor
LaNaCaMo	0.9	0.8	1.788	0.006	3.9	0.4	0.0013	0.0007	0.04
SmNaCaMo	0.0	0.8	1.791	0.006	3.7	0.4	0.0011	0.0007	0.04
YbNaCaMo	1.1	0.9	1.788	0.007	4.2	0.6	0.0023	0.0008	0.05
LaCaMo	-0.8	0.8	1.788	0.006	3.2	0.4	0.0011	0.0006	0.05
LaMo	-1.2	0.8	1.789	0.006	2.9	0.4	0.0014	0.0007	0.05

Table 4. The obtained crystalline phases and its quantitative values from XRD analysis. Estimated phase fraction errors are ~5% on the amorphous fraction and 1/4 to 2/5 of the stated value for the crystalline fractions.

Sample Name (-X)	**Powellite/$CaMoO_4$ (Mass %)**	**Oxyapatite/ $Ca_2RE_8Si_6O_{26}$ (Mass %)**	**Other (Mass %)**	**Amorphous (Mass %)**
NaCaMo	4.6	-	-	95.4
LaNaCa		9.5		90.5
LaNaCaMo	5.3	13.4		81.3
CeNaCaMo	3.3	3.9	3.1 Ceria/$Ce_{0.9}Zr_{0.1}O_2$	89.7
NdNaCaMo	5	10		85
SmNaCaMo	4.2	11.5		84.4
ErNaCaMo	3.9	13.1		83
YbNaCaMo	4.8	1.7	9.5 Keiviite/$Yb_2Si_2O_7$	84
LaCaMo	2.6			97.4
LaMo			3 Zircon/$ZrSiO_4$	97

Table 5. Quantitative analysis of powellite phases in different heat-treated samples from electron probe microanalysis (EPMA) in mass%. Values are an average of 2-3 individual measurements. Typical detection limits for each element are also reported. BDL = below detection limit, ND = not determined. Note that –X (heat treated) is not added to the names in the table but is implied. *Only one useable measurement of NaCaMo.

	LaNaCaMo		NdNaCaMo		ErNaCaMo		NaCaMo*		Detection
	Avg	StdDev	Avg	StdDev	Avg	StdDev	Avg	StdDev	Limit
MoO_3	67.6	0.2	69.7	0.9	71.0	1.5	72.0	-	0.20
SiO_2	0.56	0.39	0.29	0.12	0.30	0.06	0.37	-	0.04
ZrO_2	BDL	BDL	BDL	BDL	0.17	0.13	0.00	-	0.13
B_2O_3	ND	ND	ND	ND	ND	ND	ND	ND	ND
Al_2O_3	1.02	0.32	BDL	BDL	1.02	0.21	0.60	-	0.04
CaO	20.1	0.5	23.1	0.8	24.4	0.5	26.7	-	0.02
Na_2O	1.97	0.35	1.11	0.07	0.82	0.48	BDL	BDL	0.06
RE_2O_3	8.29	1.15	6.76	0.90	3.25	0.67	BDL	BDL	0.09
Total	99.5		101.0		100.9		99.8		

Table 6. Quantitative analysis of oxyapatite phases in different heat-treated samples from electron probe microanalysis (EPMA) in mass%. Note that, for YbNaCaMo-X, due to indistinguishable contrast and morphology, oxyapatite and keiviite phases were added and the total quantitative value averaged. Note that –X (heat treated) is not added to the names in the table but is implied. Values are an average of 7-14 individual measurements. Typical detection limits for each element are also reported. BDL = below detection limit.

	LaNaCa		LaNaCaMo		NdNaCaMo		SmNaCaMo		ErNaCaMo		YbNaCaMo		Detection
	Avg	StdDev	Avg	StdDev	Avg	StdDev	Avg	StdDev	Avg	StdDev	Avg	StdDev	Limit
MoO_3	BDL	BDL	BDL	BDL	BDL	BDL	BDL	BDL	BDL	BDL	BDL	BDL	0.15
SiO_2	20.3	0.3	19.8	0.2	19.6	0.3	19.1	0.4	18.6	0.3	27.6	0.4	0.06
ZrO_2	0.57	0.11	0.54	0.11	0.62	0.12	1.16	0.11	1.53	0.17	7.03	0.44	0.10
B_2O_3	3.18	0.17	2.81	0.17	2.38	0.11	1.87	0.17	4.68	0.33	3.49	0.26	0.10
Al_2O_3	BDL	BDL	BDL	BDL	BDL	BDL	BDL	BDL	0.48	1.38	1.18	0.67	0.06
CaO	10.24	0.39	9.75	0.21	9.38	0.18	9.48	0.20	10.17	0.45	4.75	0.47	0.02
Na_2O	BDL	BDL	0.11	0.08	BDL	BDL	BDL	BDL	BDL	BDL	BDL	BDL	0.08
RE_2O_3	66.6	0.9	66.7	0.8	68.8	0.4	67.5	0.5	66.4	5.6	57.0	3.3	0.11
Total	101.0		99.8		100.8		99.2		102.0		101.2		

Figures

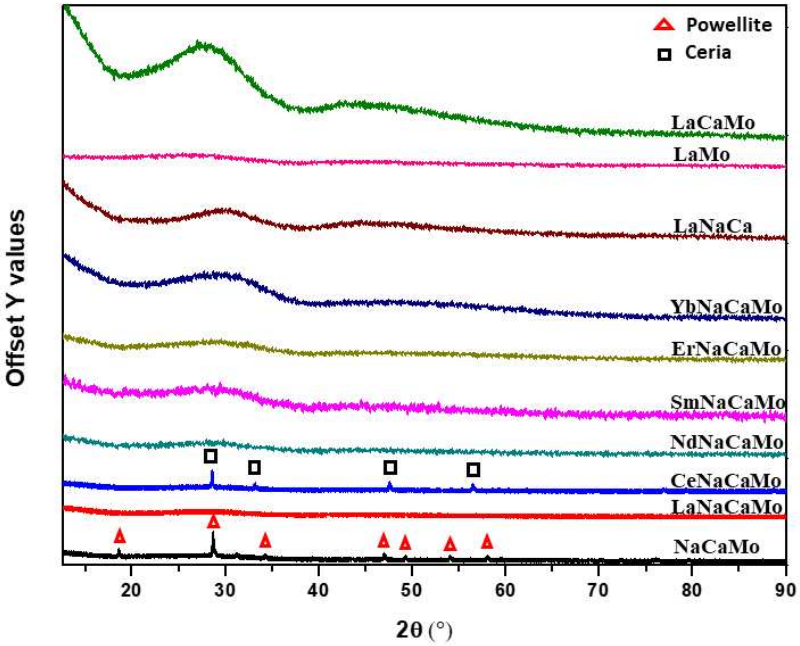

Fig. 1. XRD plot of all quenched samples (after remelt).

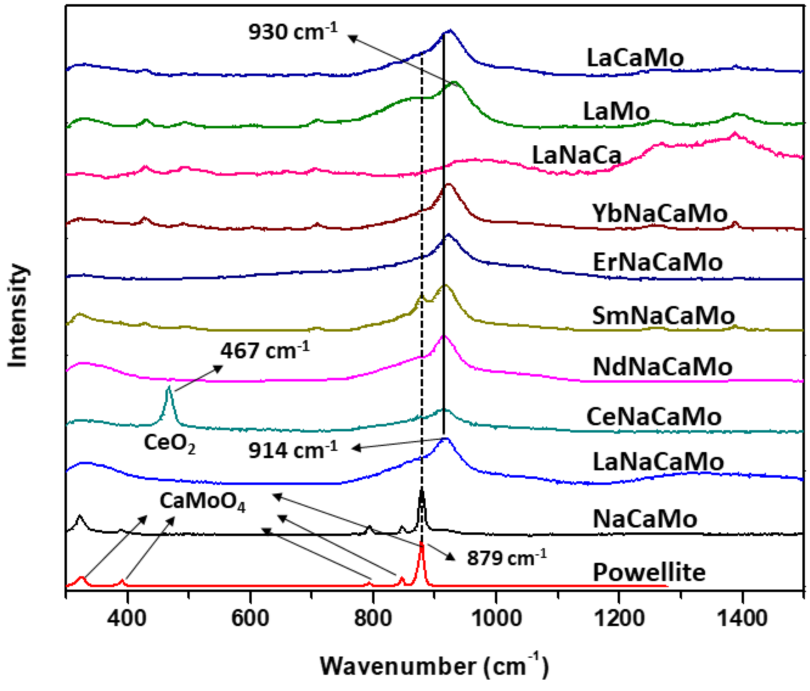

Fig. 2. Normalized Raman spectra of all samples, including a reference spectrum of $CaMoO_4$ (powellite).

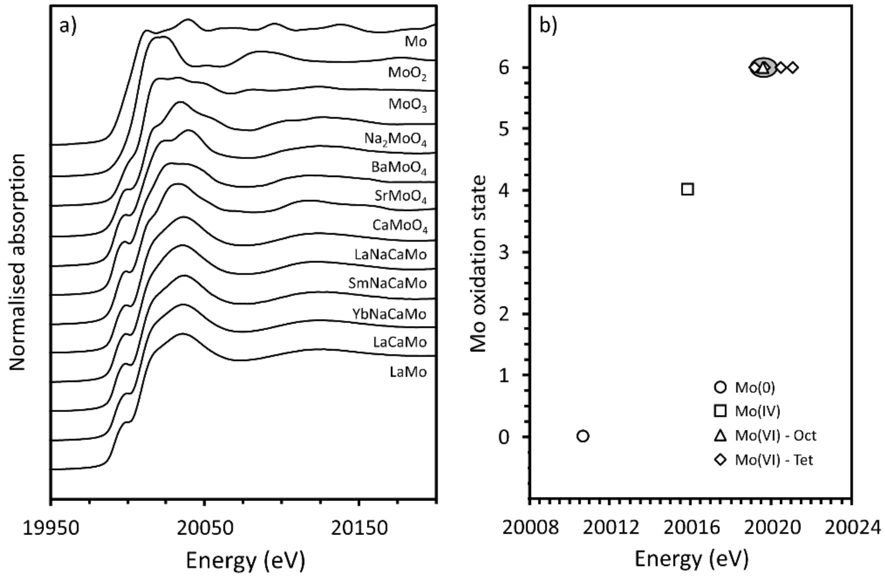

Fig. 3. Analysis of the Mo K-edge position. a) Normalized Mo K-edge XANES data for glass samples; spectra for reference standards are included. b) Relationship between the K-edge position (defined as the energy where the edge jump is equal to 0.8) and the Mo oxidation state; data points for the glass samples all sit within the grey ellipse.

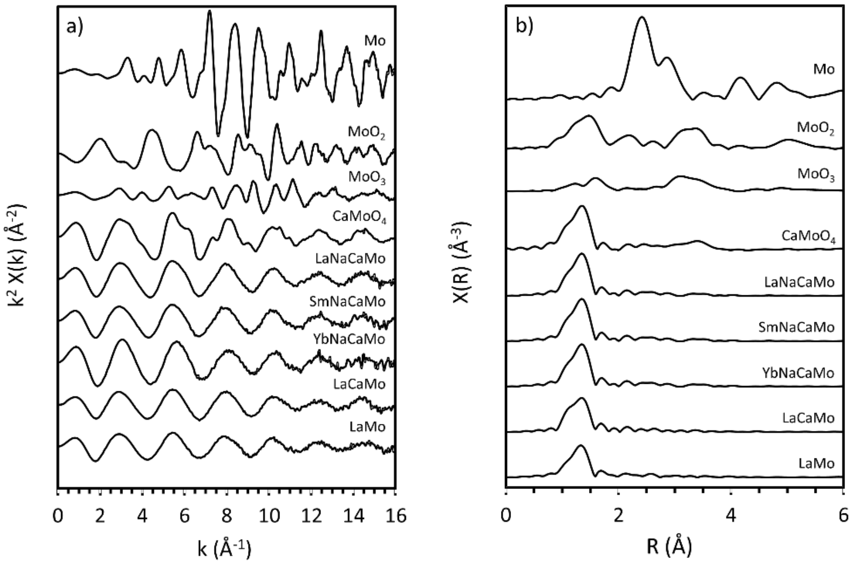

Fig. 4. EXAFS spectra for the glasses and selected reference standards. a) Normalised k^2-weighted spectra and b) Fourier transforms of k^2-weighted spectra (RDF).

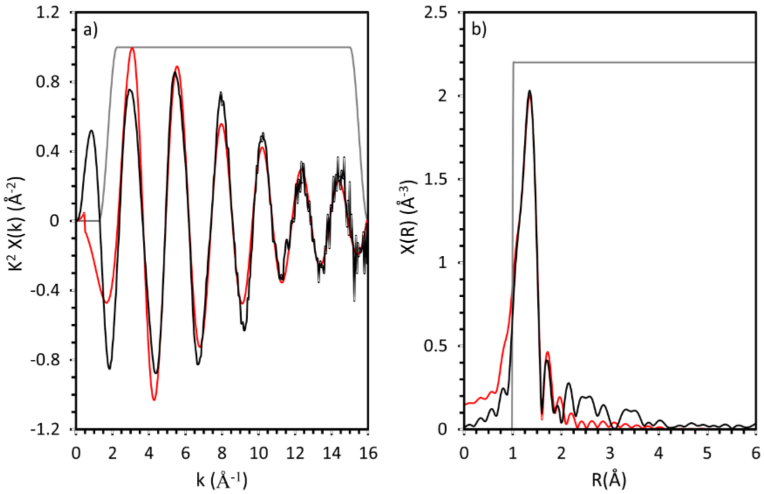

Fig 5. EXAFS spectra for LaNaCaMo; a) normalised k^2-weighted spectra and b) Fourier transforms of k^2-weighted spectra (RDF). The black line represents the experimental data and the red line represents the theoretical fit. Fitting window is indicated by solid grey line.

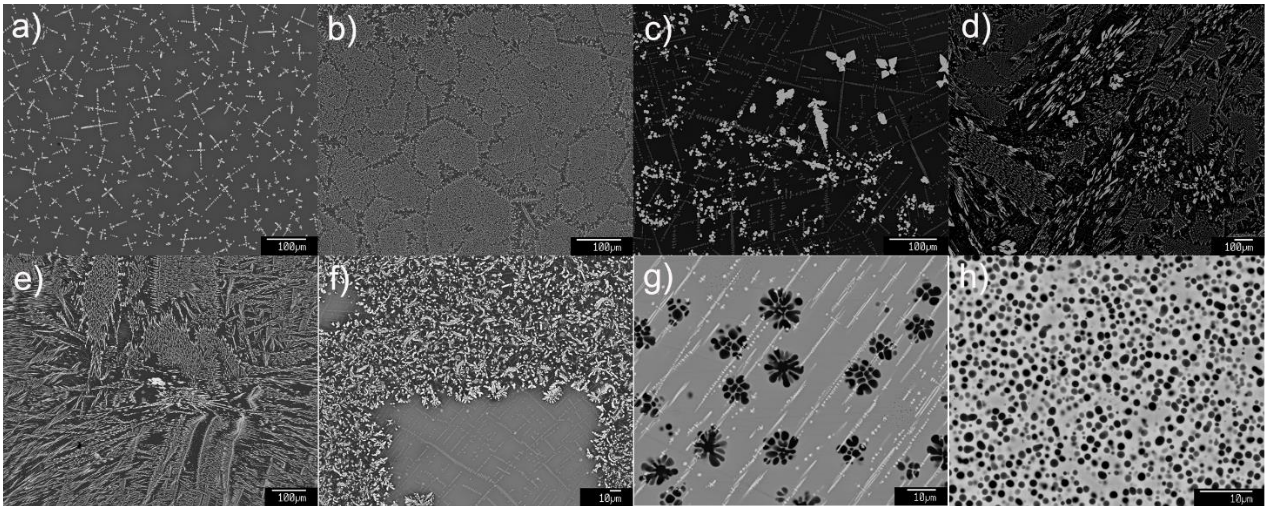

Fig. 6. BSE images of the selected samples; not different scales on some images: a) NaCaMo-X, b) LaNaCaMo-X, c) CeNaCaMo-X, d) NdNaCaMo-X, e) ErNaCaMo-X, f) YbNaCaMo-X, g) LaCaMo-X, h) LaMo-X; further images are provided in Supplementary Information.

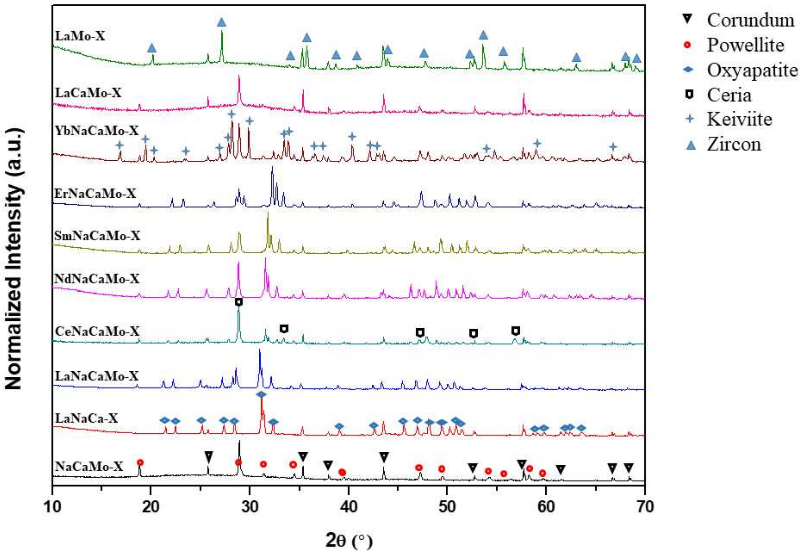

Fig. 7. XRD pattern of all heat - treated samples with corundum added as an internal reference for quantitative purpose. X-axis shows angle for Cu tube excitation.

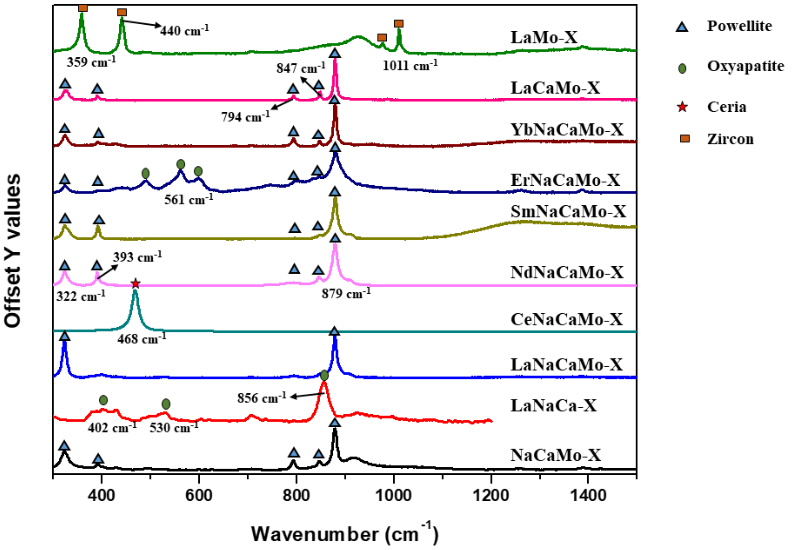

Fig. 8. Raman spectra of all heat-treated samples. The each symbol represent the characteristics peaks for corresponding phase.

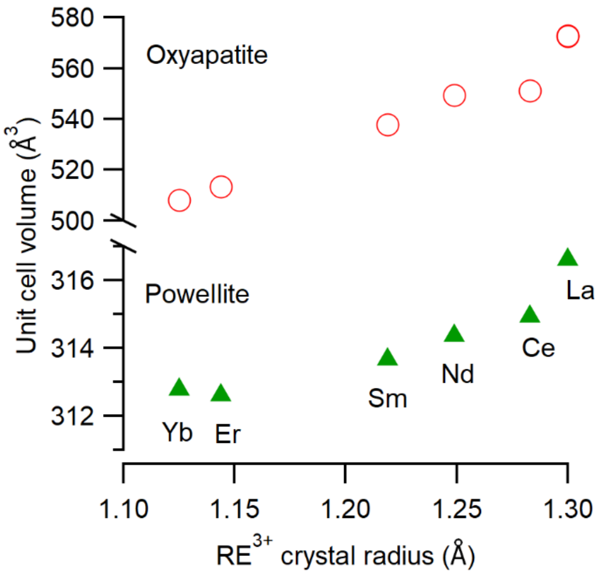

Fig. 9. Unit cell volumes of oxyapatite and powellite crystals from Rietveld refinement as a function of RE crystal radii, with coordination number 8 assumed for the RE.

Supplementary Material

Includes photos of selected samples, additional Raman and XAS details and discussion, SEM-BSE of glasses, additional SEM-BSE of glass-ceramics, EPMA analytical conditions, Rietveld refinements, and WDS maps.